Simultaneous high-resolution retinal imaging and high-penetration choroidal imaging by one-micrometer adaptive optics optical coherence tomography

Kazuhiro Kurokawa[*1,3], **Kazuhiro Sasaki**[1,3], **Shuichi Makita**[1,3], **Masahiro Yamanari**[1,3], **Barry Cense**[2,3], **and Yoshiaki Yasuno**[1,3]

[1]*Computational Optics Group in the University of Tsukuba, Tsukuba, Ibaraki, Japan*
[2]*Center for Optical Research and Education, Utsunomiya University, Utsunomiya, Tochigi, Japan*
[3]*Computational Optics and Ophthalmology Group*
yasuno@optlab2.bk.tsukuba.ac.jp

http://optics.bk.tsukuba.ac.jp/COG/

Abstract: Adaptive optics optical coherence tomography (AO-OCT) provides three-dimensional high-isotropic-resolution retinal images *in vivo*. We developed AO-OCT with a 1.03-μm probing beam and demonstrated high-penetration, high-resolution retinal imaging. Axial scans are acquired with a speed of 47,000 lines/s. AO closed loop is configured with a single deformable mirror. Seven eyes of 7 normal subjects were examined. Signal enhancement was found for all subjects. A rippled interface between nerve fiber layer and ganglion cell layer, boundary between ganglion cell layer and inner plexiform layer, and chorioscleral interface were identified. Simultaneous high-resolution and high-penetration choroidal imaging may be useful for microstructural investigation of photoreceptors and glaucomatous nerve-fiber abnormalities.

OCIS codes: (170.4500) Optical coherence tomography; (110.4500) Optical coherence tomography; (170.4460) Ophthalmic optics and devices; (110.1080) Active or adaptive optics;

References and links

1. A. F. Fercher, C. K. Hitzenberger, G. Kamp, and S. Y. El-Zaiat, "Measurement of intraocular distances by backscattering spectral interferometry," Opt. Commun. **117**, 43 – 48 (1995), http://www.sciencedirect.com/science/article/B6TVF-3XWS0W5-99/2/afffaeda4bf990ec4e44577847b7d2e8.
2. G. Hausler and M. W. Lindner, ""coherence radar" and "spectral radar"—new tools for dermatological diagnosis," J. Biomed. Opt. **3**, 21–31 (1998), http://link.aip.org/link/?JBO/3/21/1.
3. T. Mitsui, "Dynamic range of optical reflectometry with spectral interferometry," Jpn. J. Appl. Phys. **38**, 6133–6137 (1999), http://jjap.ipap.jp/link?JJAP/38/6133/.
4. R. Leitgeb, C. Hitzenberger, and A. Fercher, "Performance of fourier domain vs. time domain optical coherence tomography," Opt. Express **11**, 889–894 (2003), http://www.opticsexpress.org/abstract.cfm?URI=oe-11-8-889.
5. J. F. de Boer, B. Cense, B. H. Park, M. C. Pierce, G. J. Tearney, and B. E. Bouma, "Improved signal-to-noise ratio in spectral-domain compared with time-domain optical coherence tomography," Opt. Lett. **28**, 2067–2069 (2003), http://ol.osa.org/abstract.cfm?URI=ol-28-21-2067.
6. M. Choma, M. Sarunic, C. Yang, and J. Izatt, "Sensitivity advantage of swept source and fourier domain optical coherence tomography," Opt. Express **11**, 2183–2189 (2003), http://www.opticsexpress.org/abstract.cfm?URI=oe-11-18-2183.

7. M. Wojtkowski, T. Bajraszewski, P. Targowski, and A. Kowalczyk, "Real-time in vivo imaging by high-speed spectral optical coherence tomography," Opt. Lett. **28**, 1745–1747 (2003), http://ol.osa.org/abstract.cfm?URI=ol-28-19-1745.
8. N. Nassif, B. Cense, B. H. Park, S. H. Yun, T. C. Chen, B. E. Bouma, G. J. Tearney, and J. F. de Boer, "In vivo human retinal imaging by ultrahigh-speed spectral domain optical coherence tomography," Opt. Lett. **29**, 480–482 (2004), http://ol.osa.org/abstract.cfm?URI=ol-29-5-480.
9. B. Cense, "Optical coherence tomography for retinal imaging," Ph.D. thesis, Twente University (2005).
10. T. C. Chen, A. Zeng, W. Sun, M. Mujat, and J. F. de Boer, "Spectral domain optical coherence tomography and glaucoma." Int. Ophthalmol. Clin. **48**, 29–45 (2008), http://dx.doi.org/10.1097/IIO.0b013e318187e801.
11. G. M. Hale and M. R. Querry, "Optical constants of water in the 200-nm to 200-µm wavelength region," Appl. Opt. **12**, 555–563 (1973), http://ao.osa.org/abstract.cfm?URI=ao-12-3-555.
12. P. Schiebener, J. Straub, J. M. H. L. Sengers, and J. S. Gallagher, "Refractive index of water and steam as function of wavelength, temperature and density," Journal of Physical and Chemical Reference Data **19**, 677–717 (1990), http://link.aip.org/link/?JPR/19/677/1.
13. Y. Wang, J. Nelson, Z. Chen, B. Reiser, R. Chuck, and R. Windeler, "Optimal wavelength for ultrahigh-resolution optical coherence tomography," Opt. Express **11**, 1411–1417 (2003), http://www.opticsexpress.org/abstract.cfm?URI=oe-11-12-1411.
14. A. Unterhuber, B. Považay, B. Hermann, H. Sattmann, A. Chavez-Pirson, and W. Drexler, "In vivo retinal optical coherence tomography at 1040 nm - enhanced penetration into the choroid," Opt. Express **13**, 3252–3258 (2005), http://www.opticsexpress.org/abstract.cfm?URI=oe-13-9-3252.
15. M. Hammer, A. Roggan, D. Schweitzer, and G. Muller, "Optical properties of ocular fundus tissues-an in vitro study using the double-integrating-sphere technique and inverse monte carlo simulation," Physics in Medicine and Biology **40**, 963–978 (1995), http://stacks.iop.org/0031-9155/40/963.
16. Y. Yasuno, Y. Hong, S. Makita, M. Yamanari, M. Akiba, M. Miura, and T. Yatagai, "In vivo high-contrast imaging of deep posterior eye by 1-um swept source optical coherence tomography andscattering optical coherence angiography," Opt. Express **15**, 6121–6139 (2007), http://www.opticsexpress.org/abstract.cfm?URI=oe-15-10-6121.
17. E. C. Lee, J. F. de Boer, M. Mujat, H. Lim, and S. H. Yun, "In vivo optical frequency domain imaging of human retina and choroid," Opt. Express **14**, 4403–4411 (2006), http://www.opticsexpress.org/abstract.cfm?URI=oe-14-10-4403.
18. B. Povazay, B. Hermann, A. Unterhuber, B. Hofer, H. Sattmann, F. Zeiler, J. E. Morgan, C. Falkner-Radler, C. Glittenberg, S. Blinder, and W. Drexler, "Three-dimensional optical coherence tomography at 1050 nm versus 800 nm in retinal pathologies: enhanced performance and choroidal penetration in cataract patients." J. Biomed Opt. **12**, 041211 (2007), http://link.aip.org/link/?JBO/12/041211/1.
19. D. M. de Bruin, D. Burnes, J. Loewenstein, Y. Chen, S. Chang, T. Chen, D. Esmaili, and J. F. de Boer, "In-vivo three-dimensional imaging of neovascular age related macular degeneration using optical frequency domain imaging at 1050 nm," Invest. Ophthalmol. Vis. Sci. pp. iovs.07–1553 (2008).
20. Y. Yasuno, M. Miura, K. Kawana, S. Makita, M. Sato, F. Okamoto, M. Yamanari, T. Iwasaki, T. Yatagai, and T. Oshika, "Visualization of sub-retinal pigment epithelium morphologies of exudative macular diseases by high-penetration optical coherence tomography." Invest. Ophthalmol. Vis. Sci. **50**, 405–413 (2009), http://dx.doi.org/10.1167/iovs.08-2272.
21. B. Povazay, B. Hermann, B. Hofer, V. Kajć, E. Simpson, T. Bridgford, and W. Drexler, "Wide-field optical coherence tomography of the choroid in vivo." Invest. Ophthalmol. Vis. Sci. **50**, 1856–1863 (2009), http://dx.doi.org/10.1167/iovs.08-2869.
22. Y. Chen, D. L. Burnes, M. de Bruin, M. Mujat, and J. F. de Boer, "Three-dimensional pointwise comparison of human retinal optical property at 845 and 1060 nm using optical frequency domain imaging," J. Biomed. Opt. **14**, 024016 (2009), http://link.aip.org/link/?JBO/14/024016/1.
23. E. J. Fernández and P. Artal, "Ocular aberrations up to the infrared range: from 632.8 to 1070 nm," Opt. Express **16**, 21199–21208 (2008), http://www.opticsexpress.org/abstract.cfm?URI=oe-16-26-21199.
24. J. Liang, D. R. Williams, and D. T. Miller, "Supernormal vision and high-resolution retinal imaging through adaptive optics," J. Opt. Soc. Am. A **14**, 2884–2892 (1997), http://josaa.osa.org/abstract.cfm?URI=josaa-14-11-2884.
25. A. Roorda, F. Romero-Borja, W. J. D. III, H. Queener, T. J. Hebert, and M. C. W. Campbell, "Adaptive optics scanning laser ophthalmoscopy," Opt. Express **10**, 405–412 (2002), http://www.opticsexpress.org/abstract.cfm?URI=oe-10-9-405.
26. D. X. Hammer, R. D. Ferguson, C. E. Bigelow, N. V. Iftimia, T. E. Ustun, and S. A. Burns, "Adaptive optics scanning laser ophthalmoscope for stabilized retinal imaging," Opt. Express **14**, 3354–3367 (2006), http://www.opticsexpress.org/abstract.cfm?URI=oe-14-8-3354.
27. S. A. Burns, R. Tumbar, A. E. Elsner, D. Ferguson, and D. X. Hammer, "Large-field-of-view, modular, stabilized, adaptive-optics-based scanning laser ophthalmoscope," J. Opt. Soc. Am. A **24**, 1313–1326 (2007), http://josaa.osa.org/abstract.cfm?URI=josaa-24-5-1313.
28. D. C. Chen, S. M. Jones, D. A. Silva, and S. S. Olivier, "High-resolution adaptive optics scanning laser ophthalmoscope with dual deformable mirrors," J. Opt. Soc. Am. A **24**, 1305–1312 (2007),

http://josaa.osa.org/abstract.cfm?URI=josaa-24-5-1305.
29. M. Mujat, R. D. Ferguson, N. Iftimia, and D. X. Hammer, "Compact adaptive optics line scanning ophthalmoscope," Opt. Express **17**, 10242–10258 (2009), http://www.opticsexpress.org/abstract.cfm?URI=oe-17-12-10242.
30. B. Hermann, E. J. Fernández, A. Unterhuber, H. Sattmann, A. F. Fercher, W. Drexler, P. M. Prieto, and P. Artal, "Adaptive-optics ultrahigh-resolution optical coherencetomography," Opt. Lett. **29**, 2142–2144 (2004), http://ol.osa.org/abstract.cfm?URI=ol-29-18-2142.
31. Y. Zhang, J. Rha, R. Jonnal, and D. Miller, "Adaptive optics parallel spectral domain optical coherence tomography for imaging the living retina," Opt. Express **13**, 4792–4811 (2005), http://www.opticsexpress.org/abstract.cfm?URI=oe-13-12-4792.
32. R. Zawadzki, S. Jones, S. Olivier, M. Zhao, B. Bower, J. Izatt, S. Choi, S. Laut, and J. Werner, "Adaptive-optics optical coherence tomography for high-resolution and high-speed 3d retinal in vivo imaging," Opt. Express **13**, 8532–8546 (2005), http://www.opticsexpress.org/abstract.cfm?URI=oe-13-21-8532.
33. E. J. Fernández, B. Povazay, B. Hermann, A. Unterhuber, H. Sattmann, P. M. Prieto, R. Leitgeb, P. Ahnelt, P. Artal, and W. Drexler, "Three-dimensional adaptive optics ultrahigh-resolution optical coherence tomography using a liquid crystal spatial light modulator." Vision Research **45**, 3432–3444 (2005), http://dx.doi.org/10.1016/j.visres.2005.08.028.
34. D. Merino, C. Dainty, A. Bradu, and A. G. Podoleanu, "Adaptive optics enhanced simultaneous en-face optical coherence tomography and scanning laser ophthalmoscopy," Opt. Express **14**, 3345–3353 (2006), http://www.opticsexpress.org/abstract.cfm?URI=oe-14-8-3345.
35. E. J. Fernández, L. Vabre, B. Hermann, A. Unterhuber, B. Považay, and W. Drexler, "Adaptive optics with a magnetic deformable mirror: applications in the human eye," Opt. Express **14**, 8900–8917 (2006), http://www.opticsexpress.org/abstract.cfm?URI=oe-14-20-8900.
36. R. J. Zawadzki, S. S. Choi, S. M. Jones, S. S. Oliver, and J. S. Werner, "Adaptive optics-optical coherence tomography: optimizing visualization of microscopic retinal structures in three dimensions," J. Opt. Soc. Am. A **24**, 1373–1383 (2007), http://josaa.osa.org/abstract.cfm?URI=josaa-24-5-1373.
37. R. J. Zawadzki, B. Cense, Y. Zhang, S. S. Choi, D. T. Miller, and J. S. Werner, "Ultrahigh-resolution optical coherencetomography with monochromatic and chromaticaberration correction," Opt. Express **16**, 8126–8143 (2008), http://www.opticsexpress.org/abstract.cfm?URI=oe-16-11-8126.
38. M. Pircher, R. J. Zawadzki, J. W. Evans, J. S. Werner, and C. K. Hitzenberger, "Simultaneous imaging of human cone mosaic with adaptive optics enhanced scanning laser ophthalmoscopy and high-speed transversal scanning optical coherence tomography," Opt. Lett. **33**, 22–24 (2008), http://ol.osa.org/abstract.cfm?URI=ol-33-1-22.
39. E. J. Fernández, B. Hermann, B. Považay, A. Unterhuber, H. Sattmann, B. Hofer, P. K. Ahnelt, and W. Drexler, "Ultrahigh resolution optical coherence tomography and pancorrection for cellular imaging of the living human retina," Opt. Express **16**, 11083–11094 (2008), http://www.opticsexpress.org/abstract.cfm?URI=oe-16-15-11083.
40. R. J. Zawadzki, S. S. Choi, A. R. Fuller, J. W. Evans, B. Hamann, and J. S. Werner, "Cellular resolution volumetric in vivo retinal imaging with adaptive optics–optical coherence tomography," Opt. Express **17**, 4084–4094 (2009), http://www.opticsexpress.org/abstract.cfm?URI=oe-17-5-4084.
41. C. Torti, B. Považay, B. Hofer, A. Unterhuber, J. Carroll, P. K. Ahnelt, and W. Drexler, "Adaptive optics optical coherence tomography at 120,000 depth scans/s for non-invasive cellular phenotyping of the living human retina," Opt. Express **17**, 19382–19400 (2009), http://www.opticsexpress.org/abstract.cfm?URI=oe-17-22-19382.
42. B. Cense, W. Gao, J. M. Brown, S. M. Jones, R. S. Jonnal, M. Mujat, B. H. Park, J. F. de Boer, and D. T. Miller, "Retinal imaging with polarization-sensitive optical coherence tomography and adaptive optics," Opt. Express **17**, 21634–21651 (2009), http://www.opticsexpress.org/abstract.cfm?URI=oe-17-24-21634.
43. K. Kurokawa, D. Tamada, S. Makita, and Yoshiaki Yasuno, "Adaptive optics retinal scanner for one-micrometer light source," Opt. Express **18**, 1406–1418 (2010), http://www.opticsexpress.org/abstract.cfm?URI=oe-18-2-1406.
44. S. Makita, T. Fabritius, and Y. Yasuno, "Full-range, high-speed, high-resolution 1-μm spectral-domain optical coherence tomography using BM-scan for volumetric imaging of the human posterior eye," Opt. Express **16**, 8406–8420 (2008), http://www.opticsexpress.org/abstract.cfm?URI=oe-16-12-8406.
45. F. Jaillon, S. Makita, M. Yabusaki, and Y. Yasuno, "Parabolic BM-scan technique for full range Doppler spectral domain optical coherence tomography," Opt. Express **18**, 1358–1372 (2010), http://www.opticsexpress.org/abstract.cfm?URI=oe-18-2-1358.
46. Z136 Committee, *American National Standard for Safe Use of Lasers: ANSI Z136.1-2000* (Laser Institute of America, 2003).
47. F. C. Delori, R. H. Webb, and D. H. Sliney, "Maximum permissible exposures for ocular safety (ansi 2000), with emphasis on ophthalmic devices," J. Opt. Soc. Am. A **24**, 1250–1265 (2007), http://josaa.osa.org/abstract.cfm?URI=josaa-24-5-1250.
48. H. Hofer, P. Artal, B. Singer, J. L. Aragón and D. R. Williams, "Dynamics of the eye's wave aberration," J. Opt. Soc. Am. A **18**, 497–506 (2001), http://josaa.osa.org/abstract.cfm?URI=josaa-18-3-497.
49. T. Wilson and A. R. Carlini, "Size of the detector in confocal imaging systems," Opt. Lett. **12**, 227–229 (1987),

http://ol.osa.org/abstract.cfm?URI=ol-12-4-227.
50. E. Fernández and W. Drexler, "Influence of ocular chromatic aberration and pupil size on transverse resolution in ophthalmic adaptive optics optical coherence tomography," Opt. Express **13**, 8184–8197 (2005), http://www.opticsexpress.org/abstract.cfm?URI=oe-13-20-8184.
51. E. J. Fernández, A. Unterhuber, B. Považay, B. Hermann, P. Artal, and W. Drexler, "Chromatic aberration correction of the human eye for retinal imaging in the near infrared," Opt. Express **14**, 6213–6225 (2006), http://www.opticsexpress.org/abstract.cfm?URI=oe-14-13-6213.
52. P. Artal, S. Marcos, R. Navarro, and D. R. Williams, "Odd aberrations and double-pass measurements of retinal image quality," J. Opt. Soc. Am. A **12**, 195–201 (1995), http://josaa.osa.org/abstract.cfm?URI=josaa-12-2-195.
53. P. Bedggood, M. Daaboul, R. Ashman, G. Smith, and A. Metha, "Characteristics of the human isoplanatic patch and implications for adaptive optics retinal imaging," J. Biomed. Opt. **13**, 024008 (2008), http://link.aip.org/link/?JBO/13/024008/1.
54. A. Roorda and D. R. Williams, "Optical fiber properties of individual human cones," J. Vis. **2**, 404–412 (2002), http://journalofvision.org/2/5/4/.
55. A. Pallikaris, D. R. Williams, and H. Hofer, "The reflectance of single cones in the living human eye." Invest. Ophthalmol. Vis. Sci. **44**, 4580–4592 (2003), http://www.iovs.org/cgi/content/abstract/44/10/4580.
56. B. Vohnsen, I. Iglesias, and P. Artal, "Guided light and diffraction model of human-eye photoreceptors," J. Opt. Soc. Am. A **22**, 2318–2328 (2005), http://josaa.osa.org/abstract.cfm?URI=josaa-22-11-2318.
57. S. S. Choi, N. Doble, J. Lin, J. Christou, and D. R. Williams, "Effect of wavelength on in vivo images of the human cone mosaic," J. Opt. Soc. Am. A **22**, 2598–2605 (2005), http://josaa.osa.org/abstract.cfm?URI=josaa-22-12-2598.
58. R. S. Jonnal, J. Rha, Y. Zhang, B. Cense, W. Gao, and D. T. Miller, "In vivo functional imaging of humancone photoreceptors," Opt. Express **15**, 16141–16160 (2007), http://www.opticsexpress.org/abstract.cfm?URI=oe-15-24-16141.
59. W. Gao, B. Cense, Y. Zhang, R. S. Jonnal, and D. T. Miller, "Measuring retinal contributions to the optical stiles-crawford effect with optical coherence tomography," Opt. Express **16**, 6486–6501 (2008), http://www.opticsexpress.org/abstract.cfm?URI=oe-16-9-6486.

1. Introduction

Optical coherence tomography (OCT) has witnessed considerable developments in the last few decades. Spectral domain OCT (SD-OCT) has been demonstrated to provide three-dimensional depth-resolved information about biological samples based on optical heterodyne detection [1, 2] and higher sensitivity and higher acquisition speed than time domain OCT (TD-OCT) [3–8]. Ophthalmic OCT has been used for the diagnosis and investigation of several types of eye diseases, e.g., depth-resolved retinal images can be used to obtain a quantitative value of the nerve fiber layer (NFL) thickness that is related to neural abnormalities caused by glaucoma [9, 10].

Alternative probing beam wavelengths have been studied for applications in ophthalmic OCT. Although most ophthalmic OCTs use a center wavelength of an 840-nm probe for posterior-eye imaging, one of the attractive and promising probing beam wavelengths is 1.0-μm. The local minima of the water absorption and dispersion were located at around 1.0-μm [11–14]. The lower absorption of melanin and lower scattering of the retinal and choroidal fundus was found at 1.0-μm compared to 840-nm [15, 16]. These properties enable high-penetration retinal imaging at 1.0-μm, and ophthalmic OCT using a 1.0-μm probe is known to provide better image contrast of the deep region of the eye as compared to the 840-nm probe [16–22]. Additionally, moderate chromatic aberrations of the eye exist at the 1.0-μm wavelength band [23].

Cellular-level structural information cannot be easily obtained by conventional ophthalmic OCT, because residual ocular aberrations and eye motion deteriorate the lateral resolution of retinal images. In order to overcome these problems, dynamic compensation of ocular aberrations and high-speed image acquisition are essential. Adaptive optics (AO) technology has been used to compensate the ocular aberrations. AO has been combined with several types of conventional ophthalmic imaging devices such as a flood-illumination camera [24], scanning laser ophthalmoscope (SLO) [25–29], and OCT [30–40]. These combined techniques successfully

improved the lateral resolution of retinal images and provided cellular-level structural information of the *in vivo* retina, such as photoreceptors and microcapillaries, and blood cells. In particular, AO-OCT provides three-dimensional high isotropic resolution for *in vivo* retinal images. Latest studies on AO-OCT have demonstrated high-speed retinal imaging with speed of up to 120,000 A-lines/s [41]. Further, polarization sensitive-OCT (PS-OCT) has been combined with AO to realize the high-resolution measurement of birefringence [42].

In this study, we demonstrate high-penetration and high-resolution AO-OCT using a center wavelength of 1.03-μm by combining a SD-OCT and an AO retinal scanner [43–45].

2. Methods

2.1. AO retinal scanner

The schematic diagram of the AO retinal scanner is shown in Fig. 1. The AO retinal scanner was designed for a 1.0 μm wavelength and previously demonstrated as an AO-SLO system [43]. An 840-nm SLD light source is used as an AO beacon. An eye pupil, a deformable mirror (Mirao52d, Imagine Eyes, France), a Shack-Hartmann wavefront sensor (HASO32, Imagine Eyes), and horizontal and vertical scanners are placed at each conjugated plane with magnifications of 1×, 1.9×, 0.2×, 0.3×, and 0.5×. A horizontal resonant scanner (HS) is mounted on a coaxis galvanometric motor in the same fashion of Ref. 26. This resonant scanner has a resonant frequency of 15 kHz and is only used when the AO retinal scanner is used with SLO. The galvanometric motor is utilized for OCT slow scan. Another vertical galvanometric scanner (VS) is used for a fast scan of OCT. The residual wavefront error including the system and ocular aberrations is measured using the HASO32, which reconstructs the wavefront surfaces with a Zernike modal reconstruction algorithm and calculates root-mean-square (RMS) wavefront error. An AO closed loop runs within the measurement with an iteration frequency of 7 Hz. The magnification from the fiber tip to the retina is 0.91 for an emmetropic eye. The optical loss of the AO retinal scanner is 7 dB with a new pellicle beamsplitter at 1-μm.

In order to minimize the aberrations of the AO retinal scanner, cumulative astigmatism was canceled by the pair of vertically off-axis SMs [27, 43], as shown in Fig. 1 (a). Total residual RMS wavefront error of the system was measured to be less than 0.1 μm.

A Badal optometer is placed in front of the the eye pupil, L6 and L7, for the correction of large amount of defocus of the eye [27]. The correctable range was from -9 D to 4 D.

Chromatic aberrations of the eye between 840-nm and 1.03-μm were less than around 0.5 D [23]. The difference results in the displacement of the depth and lateral position of the focus, respectively called longitudinal chromatic aberration (LCA) and transversal chromatic aberration (TCA). Although the TCA between 840-nm and 1.03-μm results in different fields of view between 840-nm and 1.03-μm, the field of view of the system is calibrated by 1.03-μm and this TCA does not introduce a significant error. The LCA between 840-nm and 1.03-μm was canceled by adjusting the lens distance between L4 and L5.

In order to eliminate the abrupt fluctuation of aberrations caused by the pull-back action of the galvanometric scanner, the frequency of the AO closed loop was configured to be identical to a submultiple of the frequency of the galvanometric scanner. Further, HASO32 was driven by a synchronization trigger that was generated from the position monitor of the fast galvanometric scanner.

A fixation target was used to reduce the eye motion and to allow imaging of given eccentricity. As the fixation target, grid lines were printed on a paper and placed at a retinal conjugated plane. The measured eccentricity was roughly calibrated using the fixation target up to an eccentricity of 9 degrees.

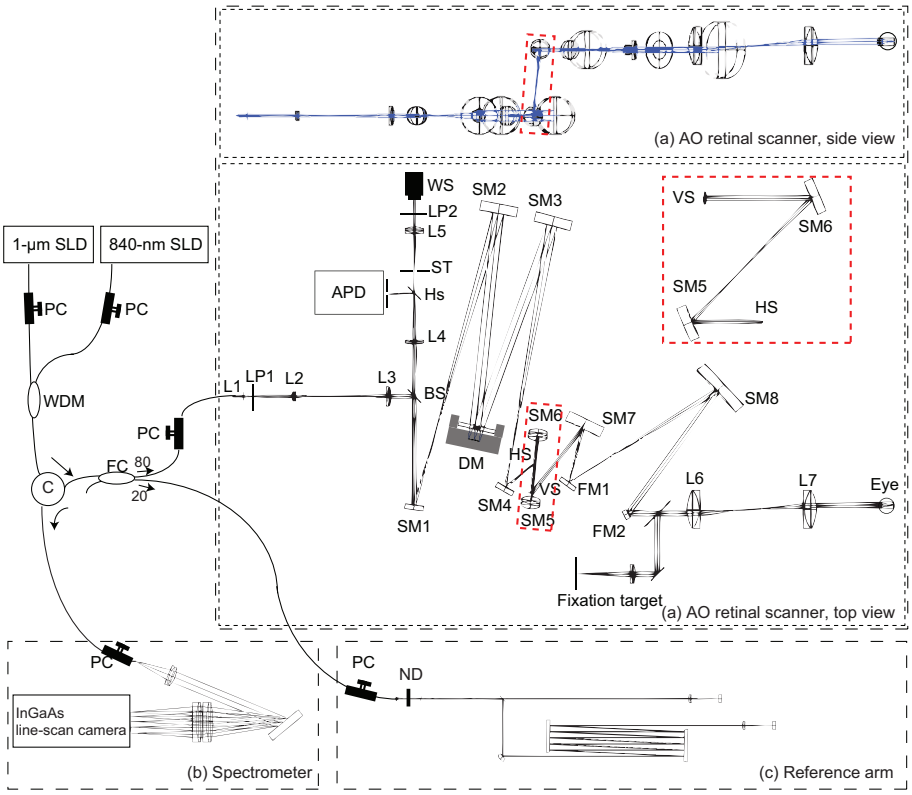

Fig. 1. Schematic of the AO-OCT. WDM: Wavelength division multiplexing coupler, C: Circulator, PC: Polarization controller, FC: Fiber coupler. (a) The side and top views of the optical setup of the AO retinal scanner. L#: Lenses, LP#: Linear polarizers, BS: Beam splitter, Hs: Harmonic separator, ST: Stop, SM#: Spherical mirrors, FM#: Flat mirrors, WS: Wavefront sensor, DM: Deformable mirror, VS: Vertical galvanometric scanner, HS: Horizontal resonant scanner mounted galvanometric scanner, APD: Avalanche photodiode. (b) Reference arm. ND: ND filter. (c) Spectrometer.

2.2. SD-OCT

The OCT system is based on an unbalanced Michelson interferometer, the schematic of which is shown in Fig. 1. The light source for the probing beam is 1-μm SLD (Superlum) with a center wavelength of 1.03-μm and a spectral bandwidth (FWHM) of 106 nm. The theoretical axial resolution was 3.4 μm in tissue, and the measured axial resolution was 5.6 μm in tissue. The 1.03-μm light is coupled with 840-nm light using a wavelength division multiplexing (WDM) coupler that was designed for 1.06-μm and 840-nm. Then, the light passes through a circulator and a fiber coupler, both of which are designed for 1.06-μm light. A polarization controller is placed before the circulator and aligned such that polarization mode dispersion is avoided; this mainly occurs at the circulator. After passing through the fiber coupler, 20% of the light is delivered to the reference arm and 80 % of the light is delivered to the AO retinal scanner.

The backscattered light from the retina is recoupled and sent back to the fiber coupler, where it is recombined with the reference signal. 80% of the recombined light is delivered to the spectrometer and collimated by an achromatic lens, diffracted by a reflective grating, and detected by an InGaAs line-scan camera with 1024-pixel resolution (SUI1024LDH, Sensors Unlimited,

Inc.) at a speed of 47,000 lines/s. A polarization controller is aligned to optimize the polarization state; this improves the efficiency of the reflection grating. The details of the SD-OCT system have been described in [44, 45].

The optical powers on the cornea was 0.9 mW for the probing beam and 0.07 mW for the AO beacon. These were below the American National Standard Institute (ANSI) safety limit [46, 47].

2.3. System sensitivity

In order to evaluate the system performance of AO-OCT, the system sensitivity was evaluated.

The sensitivity measurement was performed using a model eye with a mirror reflector at a retinal conjugated plane. During the measurement, the deformable mirror was flattened, and hence the system aberrations were not corrected. The measured sensitivity of AO-OCT was 83 dB.

In the case of non-AO SD-OCT which was described in Ref. [44, 45], but operated at a half-range mode, the sensitivity was measured to be 93.0 dB, while the theoretical shot-noise-limited sensitivity is 100.8 dB. The degradation of the system sensitivity of 7.8 dB may be because of relatively high camera noise. Since the non-AO SD-OCT and AO-OCT shares a spectrometer, this sensitivity degradation may exist also in AO-OCT.

The theoretical shot-noise-limited sensitivity of AO-OCT is 95.3 dB. Accounting for the sensitivity loss based on the camera noise, a predicted sensitivity, which is limited by the camera noise and relative intensity noise, becomes 87.5 dB, and 4.5 dB loss remains unexplained. This unexplained loss could be explained by the misalignment of the mirror reflector and the system aberration. In *in vivo* AO-OCT measurements, the signal intensity will increase more by the aberration correction (See section 3.2).

2.4. Measurement protocol

We carried out tests for the 7 eyes of 7 normal subjects. A patch of the retina at an eccentricity of approximately 6 degree on the nasal retina was scanned iteratively. The imaging retinal eccentricity was set by location of external fixation point. For the stabilization of fixation, the dominant eyes were measured. For all subjects, the measured field of view is 4.5 degree on the retina with calibration for emmetropia.

The subjects followed proper procedures before the measurement. First, two drops of 0.5% tropicamide and 0.5% phenylephrine hydrochloride were applied for pupil dilation; the subject were then made to sit in a chair and place their head on a chin rest. Second, the residual defocus for a subject was roughly compensated using the Badal optometer by monitoring the RMS wavefront error, and the subjects manually controlled the axial position of the fixation target. Third, we started to run the AO closed loop. The eye was centralized by the subject based on the direction of an operator who monitored the transversal location of the pupil by a Shack-Hartmann image. The depth position was controlled by monitoring the OCT images.

Note that the defocus of the eye was not constant in time even we applying the eye drops because of the temporal dynamics of accommodation [48]. A single OCT volume requires a measurement time of a few second. For each measurement session, the aberrations of the eye was successfully compensated with sufficiently high iteration frequency of the AO closed loop. However, between each session, the amount of defocus will become larger than the stroke of the deformable mirror. This requires the defocus correction using the Badal optometer.

Informed consent was obtained from all of the subjects. This protocol conformed to the Declaration of Helsinki, and it was approved by the Institutional Review Board of the University of Tsukuba.

3. Results

3.1. Retinal images

The effect of AO correction is shown in Fig. 2. Images without AO were obtained when the deformable mirror was flattened and the defocus of the eye was corrected using the Badal optometer. With AO correction, the residual RMS wavefront error was typically 0.1 μm. The signal strength was improved and the image contrast was enhanced. However, the improvement of the lateral resolution was not huge as compared to that observed by AO-SLO, because the lateral resolution of AO-OCT is high even without AO. This difference might be attributable to the difference in the confocality (see Section 4.1).

The averaged B-scan image shown in Fig. 3 provides better visibility of detailed structures. Five frames are averaged in a linear scale after the numerical correction of eye motion. The dynamic range of these images is 35 dB. Each layer and boundary were identified based on histology and previous studies [36, 41]. Rippled interfaces between the nerve fiber layer (NFL) and the ganglion cell layer (GCL) were identified. This may correspond to the individual nerve fiber bundles that had been difficult to resolve using non-AO SD-OCT. The boundary between GCL and the inner plexiform layer (IPL) was identified. In addition, the chorioscleral interface was identified. This appearance indicates high penetration property of 1-μm wavelength.

In general, the depth dependent intensity change is not significant using 1-μm AO-OCT in comparison to 800-nm AO-OCT. There are two possible reasons: First, the 1-μm light results in wider depth of focus. Second, our system has relatively higher LCA in comparison to 800-nm AO-OCT using an achromatizer [37, 51].

3.2. Analysis of image contrast

In order to confirm the feasibility of the system, several eyes were examined, as shown in Fig. 4. The subject's demographics are summarized in Table 1. An improvement of the image contrast was found in all subjects with AO.

In order to analyze the image contrast quantitatively, signal-to-noise ratio (SNR) and signal gains were calculated, as shown in Table 2. The SNR is defined as $10log\frac{max(I)}{\sigma^2}$. Here, $max(I)$ is the maximum intensity of the selected layers: NFL-IPL including the regions from the NFL to the IPL, INL-ONL including regions from the INL to the ONL, PRL-Choroid including regions from the PRL to the Choroid. σ^2 is a signal variance at a vitreous region which is considered as noise energy. Here, we assumed that the noise energy is constant between AO-on and AO-off. On the other hand, the signal gains were calculated as the ratio of the SNR with AO-on and the SNR with AO-off. Hence, the gain can be regarded as the gain of the signal energy. Note that the signal roll-off of the system was taking into account for the calculation. The signals were normalized by a fitting function of the measured roll-off sensitivity. As a result, positive signal gains were observed with all the subjects except NFL-IPL of subjects D and F. These negative gains are because of decreasing depth of focus by AO. Paired two-sided t-tests were performed to evaluate the gain of SNR for several depth regions. For the t-test, t.test function of a statistic language R was employed. For all 3 depth positions, statistically significant improvement of SNR was observed (P = 0.006, P = 0.004, and P = 0.014 for the regions of NFL-IPL, ONL-ONL and PRL-Choroid). The averaged signal gains were 7.0 dB, 8.2 dB, and 4.9 dB for the three depth regions, respectively.

In order to quantify the sensitivity of clinical features objectively, two OCT engineers who have more than 4-year experience in ophthalmic OCT (MY and SM) were involved as graders. The sensitivities are summarized in Table 3. The sensitivity is categorized in binary grades: 0 for invisible or +1 for visible. The targeted features are a rippled interface between the NFL, and the GCL (NFL/GCL), an interface between the GCL and the IPL (GCL/IPL), and a chorioscleral

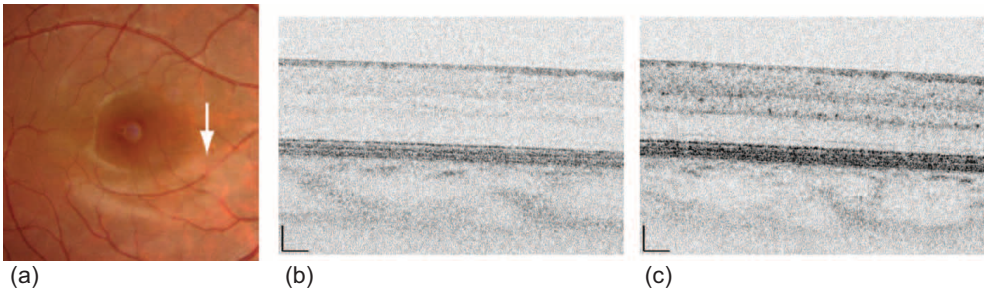

Fig. 2. (a) Color fundus photographs with the field of view of 20 degree × 20 degree. White arrow indicates the measured location of the retina. Single B-scan images (b) without AO correction and (c) with AO correction. Black bar indicates 100 μm on the retina.

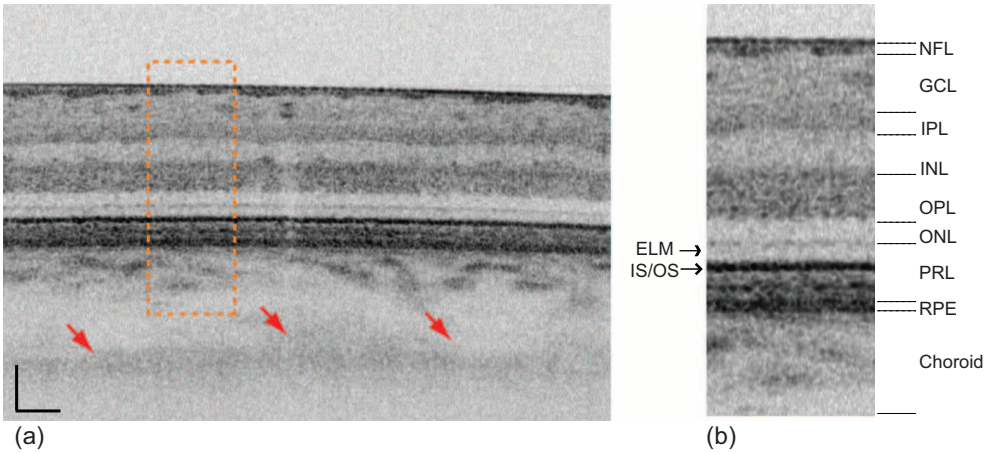

Fig. 3. Averaged B-scan image. (b) shows the region enclosed by the orange box in (a). Black bar indicates 100 μm on the retina. Red arrows indicate the chorioscleral interface. NFL: nerve fiber layer, GCL: ganglion cell layer, IPL: inner plexiform layer, INL: inner nuclear layer, OPL: outer plexiform layer, ONL: outer nuclear layer, PRL: photoreceptor layer, RPE: retinal pigment epithelium, CC: choriocapillaris, ELM: external limiting membrane, IS/OS: inner/outer segment junction.

interface (CSI). As a result, the sensitivity of NFL/GCL was 57.1% (MY and SM), that of GCL/IPL was 85.7% (MY) and 57.1% (SM), and that of CSI was 71.4% (MY and SM). The inter-grader agreements were 71.4%, 71.4%, and 100.0% for the sensitivity of the NFL/GCL, GCL/IPL, and CSI, respectively. Note that the feature of the CSI was observed with more than 71.4% and it is the advantage of high-penetration AO-OCT.

4. Discussion

4.1. Lateral resolution

In this section, we discuss the lateral resolution of AO-OCT using numerical simulations based on experimentally measured wavefront aberrations of the eye. The lateral resolution was estimated from the full width at half maximum of the point spread function (*PSF*). In confocal

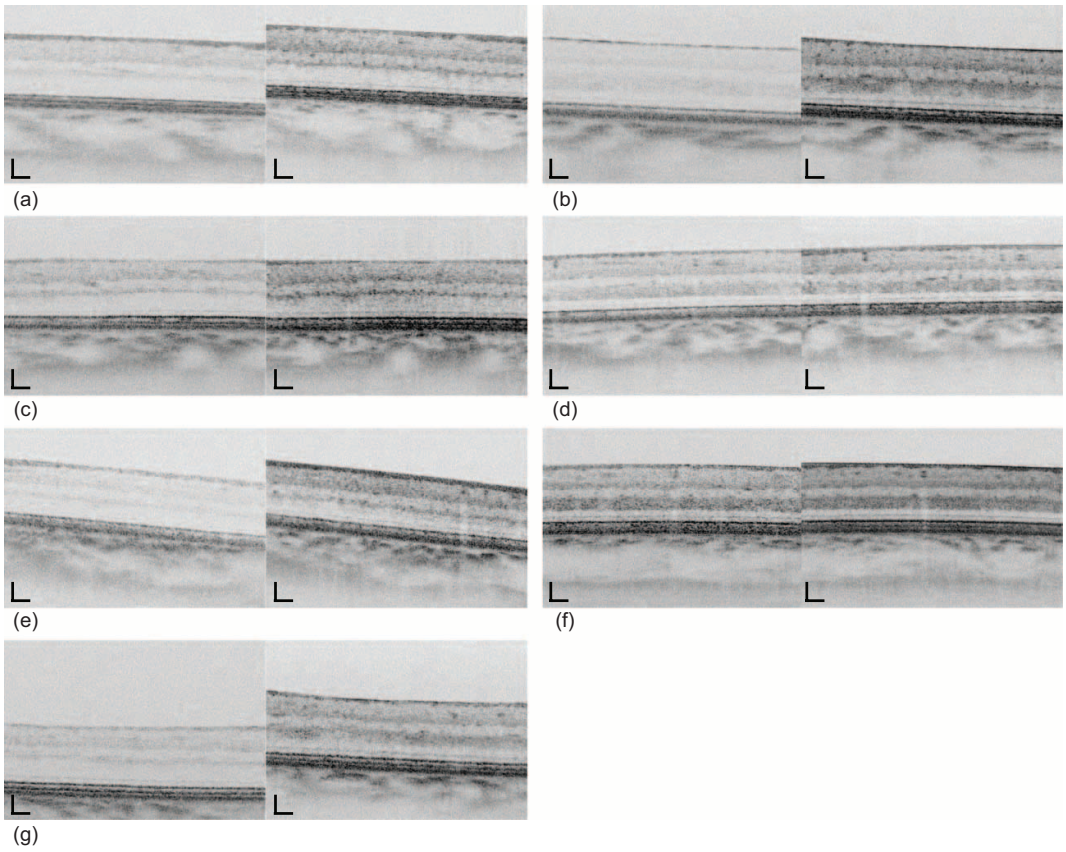

Fig. 4. Averaged B-scan images. The left part of the image was taken without AO and the right part of the image was taken with AO. (a)–(g) are corresponding with the subject ID of A–G.

microscopy, PSF is represented by the following equation [49, 50]:

$$PSF = PSF_{ill} \times (PSF_{obs} * D) \tag{1}$$

Here, PSF_{ill} and PSF_{obs} are point spread functions of illumination and observation, respectively. $*$ denotes a convolution operator. D is the finite-sized pinhole; in the case of AO-OCT, a single-mode fiber acts as a detection pinhole. We applied a Gaussian function, $D = \exp\left(\frac{X^2+Y^2}{2c^2}\right)$, to model the single-mode fiber detection. Here, c is the multiplication of the magnification and the mode field diameter of the single mode fiber, $c = \frac{(M \times D_{mode})}{4}$. In our system, $M = 0.91$ and $D_{mode} = 6\ \mu$m. Note that the $M = 0.91$ is only valid for emmetropia because M depends on the configuration of the Badal optometer. Although a similar analysis was performed by Fernández et al. [50], they did not take into account the detection pinhole and the magnification from the single-mode fiber to the retina, M, which is a function of the axial eye length if the eye is not emmetropic, i.e., M is a function of the stroke of the Badal optometer. In other words, M is used as a normalization factor between the retinal plane and the detector plane.

We used eq. (1) to estimate the lateral resolution with several magnifications, as shown in Fig. 5 (a). The curves of AO-on and AO-off were calculated on the basis of typical aberrations of a normal subject (Subject-A) measured using our AO retinal scanner while AO was turned

ID	Refractive error	Sph	Cyl	Eye (L/R)	Age
A	myopia	-6.7	-0.4	R	23
B	emmetropia	-0.3	-0.4	L	22
C	myopia	-5.6	-1.3	R	34
D	myopia	-5.4	-0.3	R	21
E	myopia	-5.9	-1.8	L	28
F	emmetropia	-0.6	-0.5	L	27
G	emmetropia	-0.3	-0.4	R	32

Table 1. Subject's characteristics. Sph and Cyl: spherical and cylindrical powers in diopter, respectively, of the eye.

ID	Signal gain [dB] NFL-IPL	Signal gain [dB] INL-ONL	Signal gain [dB] PRL-Choroid	Most signal gained layers
A	6.7	11	6.5	INL-ONL
B	7.9	10	9.3	PRL-Choroid
C	7.6	12	8.4	INL-ONL
D	-1.8	1.8	3.7	PRL-Choroid
E	13	14	5.8	INL-ONL
F	6.0	2.4	-1.7	NFL-IPL
G	9.4	6.3	2.3	NFL-IPL

Table 2. Signal gain [dB]. NFL-IPL includes the regions from the NFL to the IPL, INL-ONL includes the regions from the INL to the ONL, PRL-Choroid includes the regions from the PRL to the Choroid.

on and turned off, respectively. The residual amount of the aberration coefficients is shown in Figs. 5 (b). Fig. 5 (c) shows the evolution of the RMS wavefront error along the time course of the AO closed loop.

The lateral resolution was estimated from eq. (1). However, this analysis did not take into account the other factors that contributed to the lateral resolution, such as chromatic aberrations [37, 50, 51], underestimation of odd aberrations [52], and speckle size [42].

Although our system was operated in the 1-μm wavelength band, which has moderate chromatic aberration, the effect of chromatic aberration remained, degraded the image qualities, and results in the relatively poorer depth dependent intensity change.

Double-pass aberration measurement causes underestimation of odd aberrations of the system and the eye [52]. Namely, if the retina was regarded as an ideal scatterer (no specular reflection), the HASO32 could measure a pure single pass aberration. In practice, the light back-scattered from the retina contains the double pass information because of the specular reflection components. This becomes the error source of the aberration measurement.

The speckle size depends on the illumination diameter and the spectral bandwidth of the light source, and it degrades the image quality of the OCT images. Therefore, the actual lateral resolution is broadened to a greater extent than the estimation. For a more accurate analysis, a reasonable and reliable estimation of the lateral resolution is required.

4.2. non-AO SD-OCT vs. AO-OCT vs. AO-SLO

System performances of non-AO SD-OCT [44], AO-OCT, and AO-SLO [43] were compared, as shown in Table 4. AO-OCT provided retinal images with high isotropic resolution; however,

	Grader MY			Grader SM		
ID	NFL/GCL	GCL/IPL	CSI	NFL/GCL	GCL/IPL	CSI
A	+1	+1	+1	+1	+1	+1
B	+1	+1	0	0	0	0
C	0	0	+1	0	0	+1
D	+1	+1	+1	+1	0	+1
E	0	+1	+1	+1	+1	+1
F	+1	+1	+1	+1	+1	+1
G	0	+1	0	0	+1	0
A.S.	57.1%	85.7%	71.4%	57.1%	57.1%	71.4%

Table 3. Sensitivity of several features. The targeted features are a rippled interface between the NFL and the GCL (NFL/GCL), an interface between the GCL and the IPL (GCL/IPL), and a chorioscleral interface (CSI). A.S.: Average Sensitivity.

it had a limited field of view and lower sensitivity than the non-AO SD-OCT. The field of view is limited to an isoplanatic patch [53]. Although the problem of lower sensitivity could be overcome by the signal gain afforded by AO and the contribution of the Stiles-Crowford effect [54–59], the sensitivity of AO-OCT cannot easily exceed that of non-AO SD-OCT.

AO-OCT is expected to provide higher-resolution retinal images than AO-SLO with the advantage of higher confocality. On the other hand, the acquisition speed of AO-SLO reduces the transversal motion artifacts.

	non-AO SD-OCT	AO OCT	AO-SLO
Field of view	6 mm $\times$ 6 mm	1.3 mm	0.7 mm $\times$ 0.7 mm
Beam diameter	1.2 mm	6.5 mm	6.5 mm
Lateral resolution	21 μm	$\geq 2.9\mu$m	$\geq 3.3\mu$m
Axial resolution	3.4 μm	3.4 μm	77 μm
Measured sensitivity	93	83	–
Data acquisition speed	47,000 lines/s	47,000 lines/s	30 frames/s

Table 4. System characteristics of non-AO SD-OCT, AO-OCT, and AO-SLO.

5. Conclusion

We have demonstrated simultaneous high-penetration choroidal imaging and high-resolution retinal imaging using AO-OCT. With AO correction, this technique exhibited a statistically significant signal gain. Although the signal gain of the transversal resolution was lower than that of AO-SLO, it was sufficiently high to observe the retinal microstructures. Although non-AO-OCT with a high numerical aperture could provide moderately high resolution, the image contrast was dim, as shown in the measurement of AO-off. Therefore, the main advantage of this AO-OCT is the simultaneous realization of high-contrast and high-resolution. The retinal images provide information about not only the thickness of the retinal nerve fiber layer but also the structure of the nerve fiber. This information might be useful for carrying out a more detailed investigation of the neural abnormalities caused by glaucoma. Further, the identification of the chorioscleral interface indicates the high penetration capability of the system. This enables the investigation of microscopic structures of the deep region of the eye.

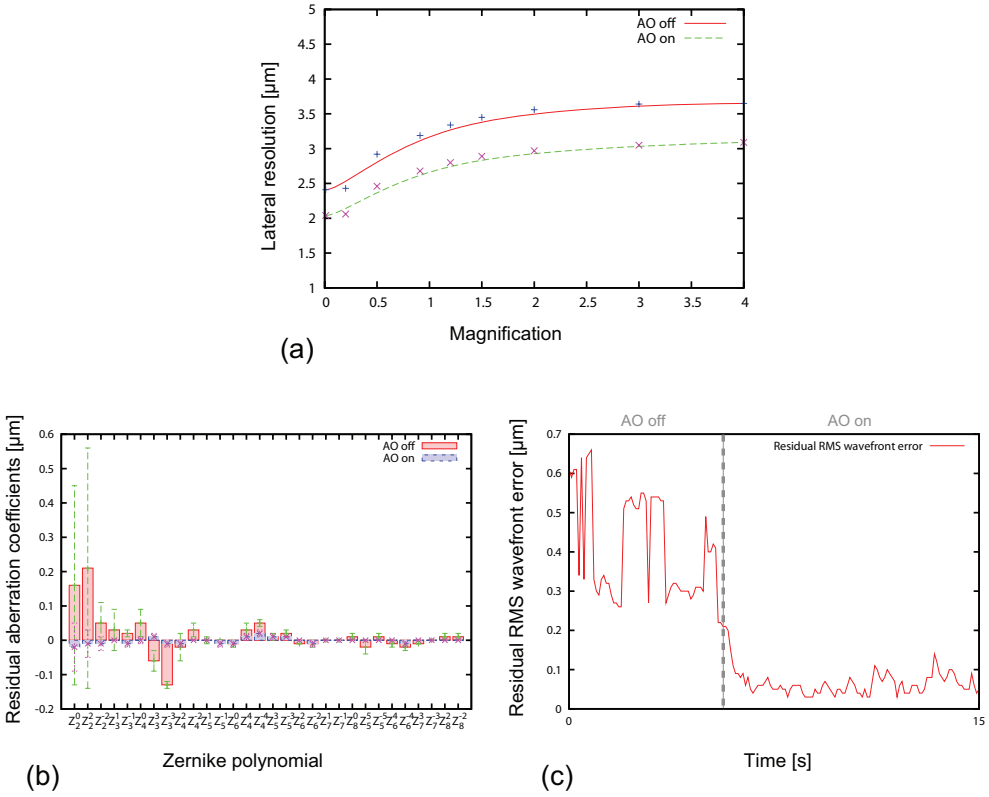

Fig. 5. (a)Lateral resolution. (b) residual aberration coefficients and (c) residual RMS wavefront error, which are measured using the HASO32. The error bars (green and red dashed lines) indicate the standard deviation of the residual aberration coefficients of AO-off and AO-on.

6. Acknowledgment

This research was supported in part by Japan Science and Technology Agency through a program of Development of Systems and Technology for Advanced Measurement and Analysis.